Nano Research

Open Access

Research Article

# Graphene aerogel for highly efficient and multifunctional EMI shielding via dielectric-magnetic synergy strategy

Xincong Du, Heguang Liu ✉, Yiwei Shao, Na Tian, and Caiyin You ✉

*School of Materials Science and Engineering, Xi'an University of Technology, Xi'an 710048, China*

**Cite this article:** *Nano Research*, **2026**, *19*, 94908554. https://doi.org/10.26599/NR.2026.94908554

**ABSTRACT:** The accelerated growth of modern electronics and devices has drawn considerable attention for the exploration and fabrication of innovative electromagnetic interference (EMI) shielding materials. Due to its layered porous architecture and distinctive characteristics, graphene aerogel is considered an appropriate candidate for advanced EMI shielding materials. Nonetheless, developing effective EMI shielding materials from graphene aerogel is challenging due to its moderate electrical conductivity. In this study, motivated by the concept of dielectric-magnetic synergy strategy, we present a graphene aerogel incorporating $CoFe_2O_4$ nanoparticles (NPs) and Ag nanowires (NWs) as enhancements. The $CoFe_2O_4$ NPs/Ag NWs/graphene aerogel, benefiting from the synergistic effects of $CoFe_2O_4$ NPs, Ag NWs, and graphene aerogel, demonstrated exceptional EMI shielding capabilities. Specifically, the $CoFe_2O_4$ NPs/Ag NWs/graphene aerogel (5 mm) offered an optimal shielding effectiveness of 67.4 dB, which was 247% of the graphite aerogel. Meanwhile, it exhibited a remarkable low density of 0.048 g/cm³ and a high specific shielding effectiveness value of up to 1291.67 dB·cm³/g. In addition, it also showed superior Joule heating performance and hydrophobicity.

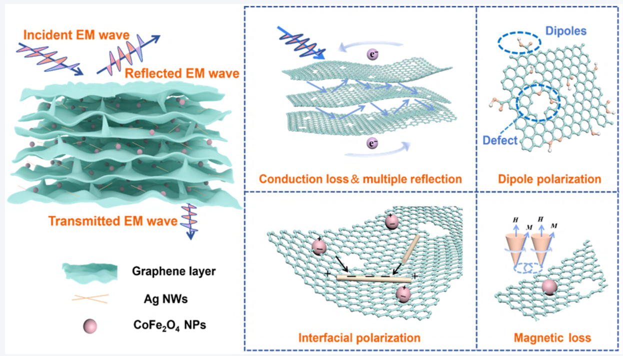


**KEYWORDS:** graphene aerogel, electromagnetic interference (EMI) shielding, Ag nanowires, $CoFe_2O_4$ nanoparticles, shielding mechanism, multifunctionality

## 1 Introduction

In recent years, rapid advancements in modern electronic technology, wireless communication, and related fields have significantly benefited people's lives, but they have also generated an enormous amount of electromagnetic waves and radiation. In particular, the widespread usage of high-frequency electrical equipment in 5G communication, artificial intelligence, and other disciplines has exacerbated the electromagnetic interference (EMI) problem [1–6]. The excessive electromagnetic waves generated by electronic equipment will not only disrupt the equipment's normal operation but may also affect individuals if exposed to high-frequency electromagnetic waves for an extended period of time. Therefore, EMI shielding materials have received an immense amount of research over the last few decades [7–13]. EMI shielding material refers to a material that can effectively block, absorb, or reflect electromagnetic waves and reduce electromagnetic interference [14–16]. In principle, this type of material can convert the electromagnetic waves in the environment into heat energy and store them in the form of micro-current, so as to reduce the electromagnetic waves in the environment.

To effectively meet the requirements of advanced electronics and devices, EMI shielding material generally needs to prioritize both high efficiency and lightweight characteristics [17–19]. Graphene aerogel is a three-dimensional porous network structure material generated by the self-assembly of graphene sheets, combining light weight, ultrahigh specific surface area, good conductivity, and good mechanical property [20–22]. The unique architecture and electromagnetic properties of graphene aerogel provide multiple reflection features and customizable shielding performance, making it ideal for a future generation of EMI shielding materials. However, due to the moderate electrical conductivity, it is difficult to achieve high shielding efficiency through pristine graphene aerogel. Recently, the synergistic effect of dielectric loss and magnetic loss has been demonstrated to be an effective strategy to achieve high shielding efficiency [23–28]. High conductive and magnetic components are reported to be employed as enhancements in

**Received:** January 6, 2026; **Revised:** February 3, 2026
**Accepted:** February 8, 2026

✉Address correspondence to Heguang Liu, heguangliu@xaut.edu.cn; Caiyin You, caiyinyou@xaut.edu.cn

graphene aerogel to achieve dielectric-magnetic synergy effect, such as carbon nanotube, $Ti_3C_2T_X$ MXene, magnetic alloy nanoparticles, ferrite nanoparticles, and so on. Nevertheless, the multifunctionality characteristic is also critical for the practical application of EMI shielding material, which can fulfill the complex application scenarios. Up to date, the study on graphene aerogel-based EMI shielding with high shielding capability and multifunctionality has been rarely reported.

In the present work, inspired by the dielectric-magnetic synergy strategy, we designed and constructed a highly efficient and multifunctional EMI shielding composite composed of graphene aerogel, Ag nanowires (NWs), and $CoFe_2O_4$ nanoparticles (NPs). Experimentally, Ag NWs and $CoFe_2O_4$ NPs were synthesized by the solvothermal method and the hydrothermal method, respectively. The incorporation of Ag NWs and $CoFe_2O_4$ NPs significantly enhanced the graphene aerogel's EMI shielding capability and endowed it with superior multifunctionality. Contributed by internal multiple reflection, interfacial polarization, Ohmic loss, and magnetic loss, the $CoFe_2O_4$ NPs/Ag NWs/graphene aerogel (5 mm) achieved a maximum shielding effectiveness (SE) of 67.4 dB in the X band. Moreover, the $CoFe_2O_4$ NPs/Ag NWs/graphene aerogel also delivered remarkable multifunctionality involving hydrophobicity and Joule heating.

## 2 Experimental

### 2.1 Synthesis of Ag NWs

Ag NWs were prepared by the solvothermal method using silver nitrate, ethylene glycol, and polyvinyl pyrrolidone (PVP). Specifically, 0.8 g PVP ($M_W$ = 1,300,000) was dissolved in 20 mL of ethylene glycol, which was thoroughly stirred. Meanwhile, 0.6794 g silver nitrate and 0.7 mg sodium chloride were added to 20 mL of ethylene glycol, which was thoroughly stirred to dissolve them evenly. Finally, the foregoing two solutions were properly mixed and agitated before being transferred to a 50 mL stainless steel reactor, heated to 160 °C for 2 h, and allowed to cool naturally. Centrifugation and repeated washing with deionized water and acetone resulted in the gray precipitate, which was then dried to collect the Ag NWs.

### 2.2 Fabrication of $CoFe_2O_4$ NPs

The hydrothermal technique was utilized to fabricate $CoFe_2O_4$ NPs. Initially, ferric nitrate (8.08 g) and cobalt nitrate (2.91 g) were mixed together in 100 mL of deionized water and magnetically agitated for 30 min. To achieve a pH of 9, add 25% ammonium hydroxide dropwise to the combined solution and stir. The resulting solution was then ultrasonically dispersed for 3 h to ensure equal distribution. After ultrasonic dispersion, the combined solution was transported to the stainless steel reactor for reaction (180 °C, 12 h). Following the reaction, the product was centrifuged and washed multiple times with deionized water and ethanol. Subsequent to drying at 60 °C for 12 h, it was heated up to 400 °C for 6 h to produce $CoFe_2O_4$ NPs.

### 2.3 Fabrication of graphene composite aerogel

Graphene oxide was fabricated via Hummer's method. Typically, for the initial step, $NaNO_3$ (1 g) and flake graphite (1 g) were mixed in a glass container. 40 mL of concentrated $H_2SO_4$ was added, and the resulting mixture was placed in an ice bath. The mixture was stirred while the temperature was kept below 20 °C. Subsequently, 5 g of $KClO_4$ was slowly added to the mixed solution and stirred thoroughly. Then, 3 g of $KMnO_4$ was introduced into the solution, which was maintained below 20 °C and stirred for 2 h. Upon completion of the low-temperature reaction, the ice-water bath was removed. The beaker was sealed with plastic wrap to prevent airborne water vapor from affecting the oxidation reaction, and the solution was stirred at room temperature (above 20 °C) for 24 h. After the moderate-temperature reaction, 40 mL of deionized water was added to the mixture, followed by stirring for 30 min. After the high-temperature reaction, an appropriate amount of $H_2O_2$ was added to the mixed solution. The system was stirred uniformly until the solution turned bright yellow to remove the excess oxidant. Finally, when the reaction was completed, the combined solution was transferred to a centrifuge tube and washed twice with 5% HCl solution before being washed several times using deionized water until the pH became 7. The supernatant was discarded, and graphene oxide was produced by freeze-drying.

Then 0.225 g of graphene oxide was dispersed in 10 mL deionized water, along with 0.0675 g of Ag NWs. The mixture was magnetically agitated for 2 h before being ultrasonically treated for another 2 h to ensure that it was evenly dispersed, yielding solution 1. Then, 0.0675 g of $CoFe_2O_4$ NPs were sonicated in 5 mL deionized water for 35 min to guarantee an even distribution, yielding solution 2. To create a $CoFe_2O_4$/Ag nanowire/graphene oxide aqueous dispersion, the two solutions were combined and stirred with a glass rod for 5 min. The dispersion was then poured into a mold, rapidly cooled using liquid nitrogen, and freeze-dried for 48 h, obtaining a graphene oxide composite aerogel. Lastly, the dried graphene oxide composite aerogel was heated at 1000 °C to create $CoFe_2O_4$/Ag NWs/graphene aerogel. For comparison, the pristine graphene aerogel and Ag NWs/graphene aerogel were also prepared.

### 2.4 Characterization

The microstructure of the obtained specimen was studied utilizing X-ray diffraction (XRD, DX-2700BH). The morphology of the samples was analyzed by scanning electron microscopy (SEM, Zeiss Merlin Compact). The samples' microstructure and morphology were investigated utilizing transmission electron microscopy (TEM, JEM-3010). The specimens' electrical conductivity was evaluated using a four-probe resistance meter (RTS-8). The samples' ultimate electrical conductivities were estimated by averaging the results of several tests. The magnetic characteristics of the materials were evaluated with a vibrating sample magnetometer (VSM, Lake Shore 7404 Mode).

The waveguide approach was applied to determine samples' EMI shielding ability. The relevant electromagnetic characteristics were obtained employing a vector network analyzer (VNA, E5071C). To fit the sample holder cavity, the samples were sliced into rectangles measuring 22.86 mm × 10.16 mm and 5 mm in thickness. The test range was operated at the frequencies ranging from 8.2 to 12.4 GHz (X-band). And the SE of the samples was calculated based on the undermentioned formulas

$$T = |S_{21}|^2 \tag{1}$$

$$R = |S_{11}|^2 \tag{2}$$

$$\mathrm{SE_A} = -10\lg(T/(1-R)) \tag{3}$$

$$\mathrm{SE_R} = -10\lg(1-R) \tag{4}$$

$$\mathrm{SE_T} = -10\lg T \tag{5}$$

where $SE_A$ represents the absorption shielding effectiveness, $SE_R$ signifies the reflection shielding effectiveness, and $SE_T$ means the total shielding effectiveness. At the same time, $T$ means transmission coefficients while $R$ represent reflection coefficients.

The sample's Joule heating performance was assessed employing a DC power source (UTP 1310), and its temperature was detected with an infrared thermal imaging camera (Fotric 628C). We used an optical contact angle meter (SDC-200, Dingsheng) to measure the contact angles (CAs) of 5 μL water droplets on the sample surface to evaluate hydrophilicity.

## 3 Results and discussion

Figure 1(a) illustrates that the $CoFe_2O_4$ NPs/Ag NWs/graphene aerogel was constructed by a freeze-drying and annealing process from the mixed aqueous suspension of graphene oxide, $CoFe_2O_4$ NPs, and Ag NWs. Experimentally, graphene oxide, Ag NWs, and $CoFe_2O_4$ NPs were fabricated respectively. Figure 1(b) displays the TEM image of the graphene oxide synthesized from flake graphite (Fig. S1 in the Electronic Supplementary Material (ESM)) using Hummer's approach [29, 30]. One could observe that the graphene oxide generated by oxidant stripping has a typical layered structure and a relatively modest thickness. To obtain the graphene layer, the graphene oxide went through a heat treatment of 1000 °C. The Raman spectra of the obtained graphene layer is demonstrated in Fig. 1(c). The graphene sample possesses representative graphite's Raman peaks, including the D and G peaks. After calculation, the value of $I_D/I_G$ is approximately 1.23, which implies the presence of defect [31].

Figures 1(d) and 1(e) depict the TEM images of Ag NWs and $CoFe_2O_4$ NPs, respectively. The obtained Ag NWs possess a typical wire morphology with a diameter around 50 nm. The XRD pattern (Fig. S2 in the ESM) clearly reveals diffraction peaks at 38.1°, 44.3°, 64.5°, and 77.5°, corresponding to the (111), (200), (220), and (311) crystal planes (PDF #04-0783) [32, 33]. The diffraction peaks of the as-prepared $CoFe_2O_4$ NPs (Fig. S3 in the ESM) at 35.4°, 56.9°, and 62.6° are ascribed to the crystal planes (311), (511), and (440) in the PDF card (PDF #22-1086), respectively [34, 35]. This indicates that the obtained $CoFe_2O_4$ sample has a cubic spinel structure. The XRD

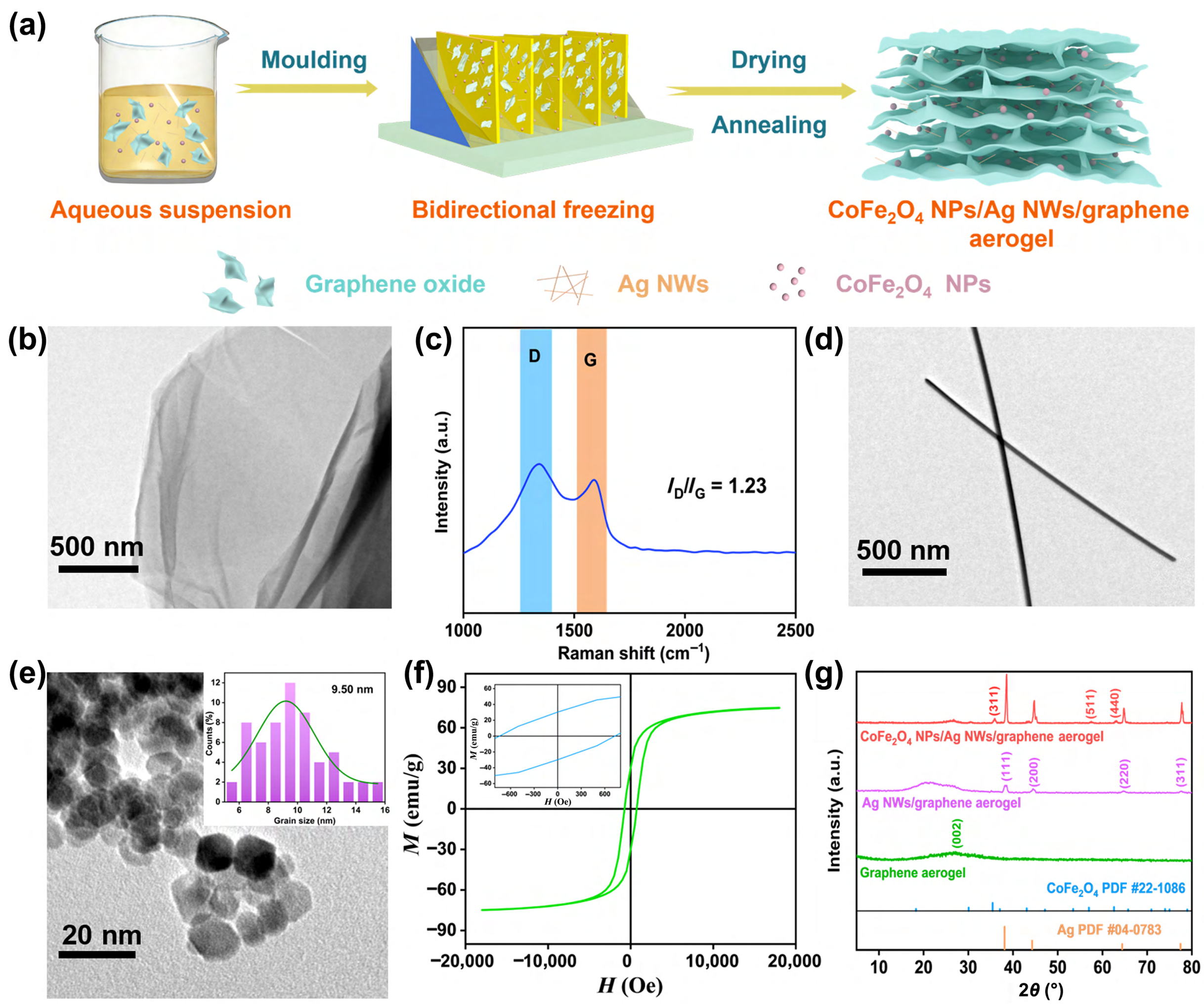


**Figure 1** (a) Schematic of the synthesis procedure of the $CoFe_2O_4$ NPs/Ag NWs/graphene aerogel. (b) TEM image of the graphene oxide nanosheet. (c) Raman spectrum of the graphene layer. TEM images of (d) the Ag NWs and (e) the $CoFe_2O_4$ NPs. (f) Hysteresis loop of the $CoFe_2O_4$ NPs. (g) XRD patterns of the graphene aerogel, Ag NWs/graphene aerogel, and $CoFe_2O_4$ NPs/Ag NWs/graphene aerogel.

pattern shows clear diffraction peaks and no impurity peaks, demonstrating the effective preparation of $CoFe_2O_4$ NPs with high crystallinity. The TEM image (Fig. 1(e)) demonstrates the size of $CoFe_2O_4$ NPs is around 10 nm. At the same time, the magnetic property of $CoFe_2O_4$ NPs is also characterized, as presented in Fig. 1(f). Specifically, the sample demonstrates good ferromagnetism, featuring a saturation magnetization ($M_s$) of 74.8 emu/g, a remanent magnetization ($M_r$) of 30.4 emu/g, and a coercivity ($H_c$) of 750 Oe. It is believed that the magnetization behavior of $CoFe_2O_4$ NPs is associated with the variation in the exchange contact between tetrahedral and octahedral sub-lattices.

In this work, to reveal the influence of Ag NWs and $CoFe_2O_4$ NPs on the graphene's performance, the pristine graphene aerogel and Ag NWs/graphene aerogel were also synthesized, respectively. As demonstrated in Fig. 1(g), the amorphous diffraction peak at 26.4° corresponds to the (002) crystal plane of reduced graphene oxide. At the same time, the characteristic peaks of Ag NWs appear at 77.5°, 44.3°, and 38.1°, corresponding to their (311), (200), and (111) crystal planes, respectively. Moreover, the characteristic peaks of $CoFe_2O_4$ NPs appear at 30.2°, 57.2°, and 62.9°, corresponding to their (311), (511), and (440) crystal planes, respectively. This indicates the fact that the heat treatment reduces the graphene oxide aerogel but not the Ag NWs or $CoFe_2O_4$ NPs, according to the XRD pattern. In other words, Ag NWs and $CoFe_2O_4$ NPs were successfully integrated into graphene aerogel. The microstructure of the as-prepared aerogel samples is displayed in Fig. 2. Figures 2(a) and 2(b) present the SEM images of graphene oxide aerogel and graphene aerogel. The graphene oxide aerogel sample has a typical layered porous structure. The formation of this architecture is highly dependent on the freeze-drying process. Because of the wedge-shaped polydimethylsiloxane (PDMS) between the copper plate base and the graphene aqueous dispersion, when liquid nitrogen is added, there is a temperature difference between the PDMS's bottom and top, and ice crystals preferentially nucleate at the bottom of the PDMS. Meanwhile, the temperature difference causes two temperature gradients in the horizontal and vertical axes, and ice crystals form along the two squares. The graphene oxide in the dispersion will also be ordered along the ice crystals' development direction until the graphene oxide aqueous dispersion is fully frozen [36, 37]. This layered porous structure remains intact after the heat treatment. Figures 2(c)–2(f) present the SEM photos of Ag NWs/graphene aerogel and $CoFe_2O_4$ NPs/Ag NWs/graphene aerogel. One could observe that the Ag NWs and $CoFe_2O_4$ NPs achieve a relatively uniform dispersion in the graphene aerogel

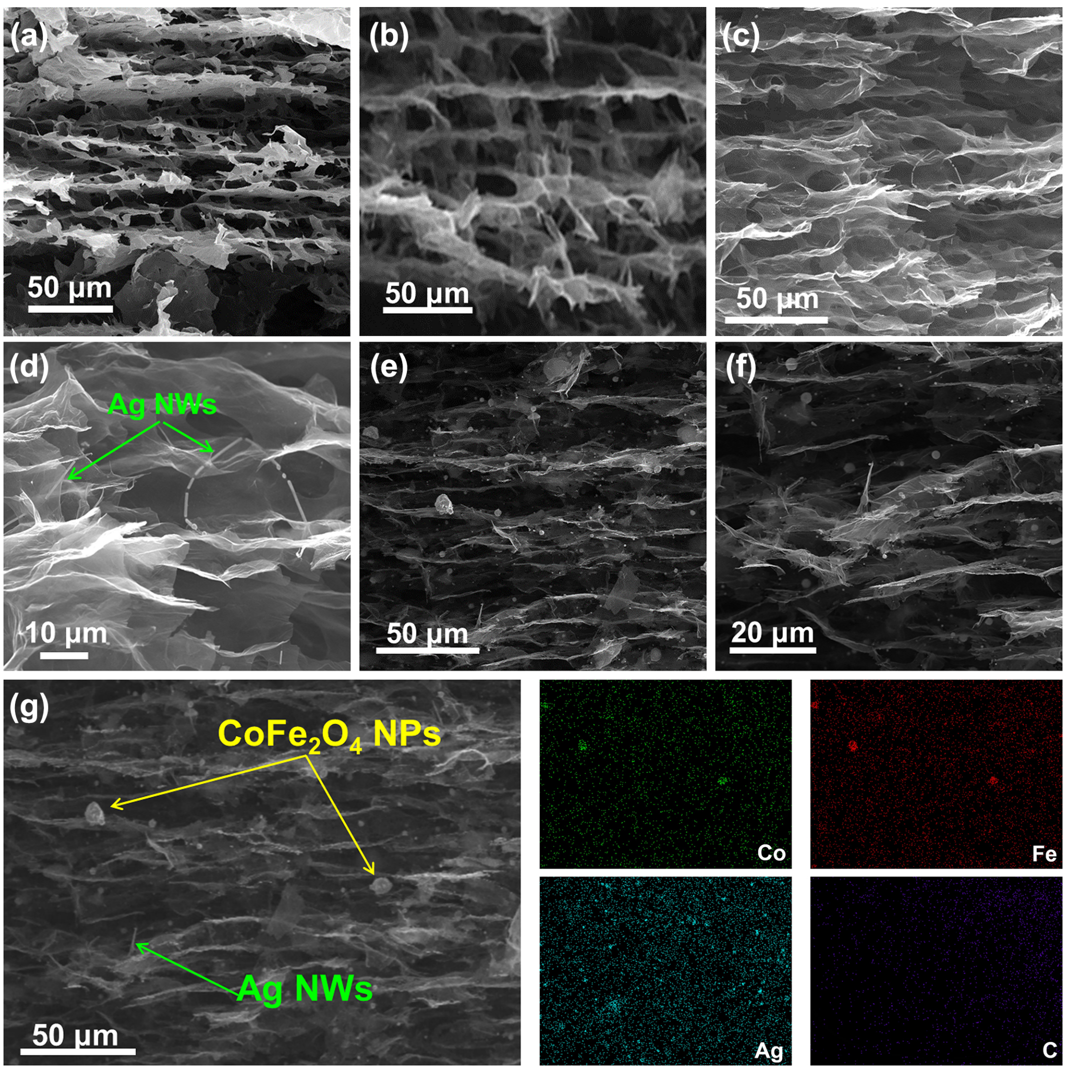


**Figure 2** SEM images of (a) the graphene oxide aerogel and (b) graphene aerogel. (c) SEM image and (d) enlarged SEM image of the Ag NWs/graphene aerogel. (e) SEM image and (f) enlarged SEM image of the $CoFe_2O_4$ NPs/Ag NWs/graphene aerogel. (g) EDS mapping of the $CoFe_2O_4$ NPs/Ag NWs/graphene aerogel.

matrix. The energy dispersive X-ray spectroscopy (EDS) mapping (Fig. 2(g)) further reveals the dispersion of the Co, Fe, Ag, and C elements.

The obtained samples' electrical conductivity is displayed in Fig. 3(a). It is obvious that the composite aerogel's electrical conductivity demonstrates significant variation with the incorporation of Ag NWs and $CoFe_2O_4$ NPs. Ag NWs have a high carrier density and electron mobility, allowing them to generate new electron transmission channels in graphene aerogels, reduce electron scattering, and create a new conductive network [38]. As a result, the conductivity of the composite aerogel rises with the addition of Ag NWs. After the addition of $CoFe_2O_4$ NPs, the $CoFe_2O_4$ NPs/Ag NWs/graphene aerogel delivers a lower electrical conductivity than that of the Ag NWs/graphene aerogel. This can be explained by the intrinsic low conductivity of $CoFe_2O_4$ NPs. The samples' electromagnetic parameters in the X-band were collected by the waveguide technique [39–41]. The shielding effectiveness is calculated based on the corresponding electromagnetic parameters. Figures 3(b)–3(d) display the SE value of the obtained samples (5 mm), including $SE_A$, $SE_R$, and $SE_T$. One could observe that the Ag NWs/graphene aerogel exhibits better EMI shielding performance than graphene aerogel. The $SE_A$ and $SE_T$ of graphene aerogel are 24.5 and 27.3 dB, respectively. At the same time, its $SE_R$ value is around 4 dB. The good electromagnetic shielding performance is due to the layered porous architecture, which not only provides enough interface for multiple reflections of electromagnetic waves but also provides a path for electron transmission between layers and takes into account the transmission between the core layer and the layer [42–44]. On the other hand, the heat treatment successfully eliminates oxygen-containing functional groups and imperfections from the graphene structure, making it more ordered and prone to electron transmission and consumption. With the addition of Ag NWs and $CoFe_2O_4$ NPs, the composite aerogel's EMI shielding performance is enhanced gradually. Specifically, the Ag NWs/graphene aerogel delivers a $SE_T$ of 52.7 dB, while the $CoFe_2O_4$ NPs/Ag NWs/graphene aerogel achieves a $SE_A$ of 48.1 dB and a $SE_T$ of 67.4 dB. Accordingly, the $CoFe_2O_4$ NPs/Ag NWs/graphene aerogel exhibits much better EMI shielding performance than that of graphene aerogel and Ag NWs/graphene aerogel. Incorporating $CoFe_2O_4$ NPs into the composite aerogel reduces conductivity but improves electromagnetic wave reflection through magnetic resonance and hysteresis loss. At the same time, $CoFe_2O_4$ NPs increase electromagnetic wave absorption by introducing eddy current loss and stronger interfacial polarization [45, 46]. Besides, the obtained aerogel samples feature low reflection shielding effectiveness, as demonstrated in Fig. 3(e). This helps to

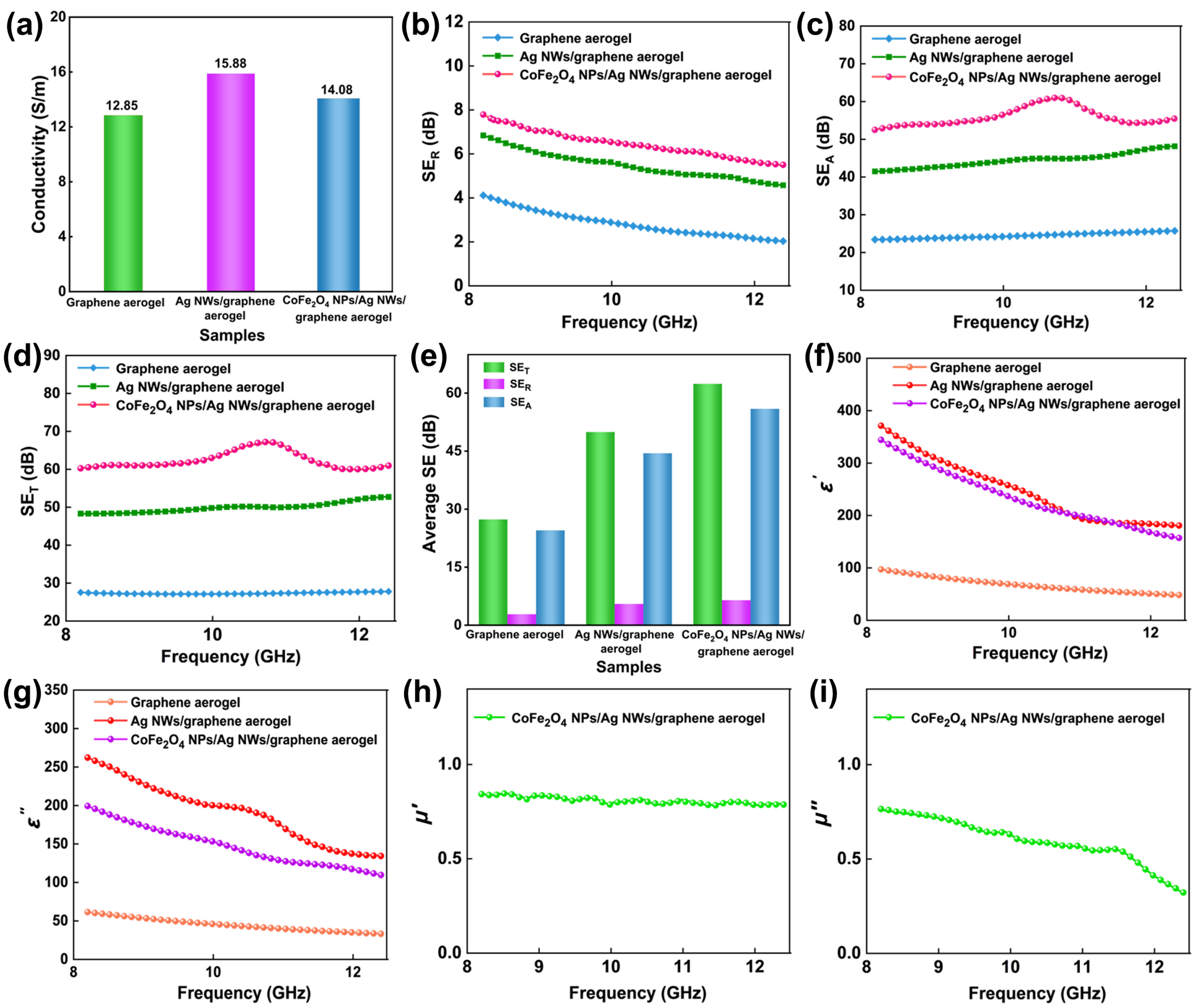


**Figure 3** (a) Electrical conductivity, (b) $SE_R$, (c) $SE_A$, (d) $SE_T$, (e) average SE, (f) $\varepsilon'$, and (g) $\varepsilon''$ of the as-prepared aerogel samples. (h) $\mu'$ and (i) $\mu''$ of the $CoFe_2O_4$ NPs/Ag NWs/graphene aerogel.

prevent the secondary electromagnetic pollution.

The samples' complex permittivity and permeability are examined for better understanding of their electromagnetic interference shielding efficacy. Figures 3(f) and 3(g) show the real component ($\varepsilon'$) and imaginary component ($\varepsilon''$) of the complex permittivity of the samples, respectively. As we all know, $\varepsilon'$ suggests capacitive energy storage, while $\varepsilon''$ implies polarization loss in electric fields [47, 48]. It can be clearly seen that the Ag NWs/graphene aerogel and $CoFe_2O_4$ NPs/Ag NWs/graphene aerogel have much higher $\varepsilon'$ and $\varepsilon''$ than that of graphene aerogel. The addition of Ag NWs boosts the concentration of free electrons in aerogel, improving its responsiveness to alternating electric fields and enhancing $\varepsilon'$. Additionally, heterogeneous interfaces such as Ag/carbon, $CoFe_2O_4$/silver, and $CoFe_2O_4$/carbon promote interfacial polarization, with electrons accumulating at the contact to form dipoles. An alternating electric field causes dipoles to orient and polarize, leading to a rise in $\varepsilon''$. The real component ($\mu'$) and imaginary component ($\mu''$) of the complex permeability of the $CoFe_2O_4$ NPs/Ag NWs/graphene aerogel are measured, as shown in Figs. 3(h) and 3(i). $\mu'$ describes capacitive energy storage, and $\mu''$ denotes polarization loss within magnetic fields [49, 50]. The addition of $CoFe_2O_4$ NPs improves graphene aerogel's magnetic response, providing the composite aerogel with both real and imaginary permeability. This suggests that the addition of $CoFe_2O_4$ NPs can improve the permeability of the composite aerogel and enrich its loss mechanism to electromagnetic waves. The composite aerogel can absorb electromagnetic waves more effectively owing to the magnetic-dielectric synergistic effect, which corresponds to an increase in shielding effectiveness shown in Fig. 3(e).

The samples' attenuation constant ($\alpha$) and skin depth ($\delta$) are also studied to further evaluate their EMI shielding performance, as depicted in Figs. 4(a) and 4(b). Compared to graphene aerogel and Ag NWs/graphene aerogel, the $CoFe_2O_4$ NPs/Ag NWs/graphene aerogel delivers a higher α and a lower $\delta$. This further confirms the excellent EMI shielding property of the $CoFe_2O_4$ NPs/Ag NWs/graphene aerogel. At the same time, the density of the $CoFe_2O_4$ NPs/Ag NWs/graphene aerogel is only 0.048 g/cm$^3$. According to the calculation, the $CoFe_2O_4$ NPs/Ag NWs/graphene aerogel delivers a specific shielding effectiveness (SSE) of 1291.67 dB·cm$^3$/g. The electromagnetic shielding efficacy of the composite aerogel developed in this work surpasses that of many other graphene aerogel materials reported previously (Fig. 4(c)) [51–59]. Figure 4(d) depicts the EMI shielding mechanism of the $CoFe_2O_4$ NPs/Ag NWs/graphene aerogel based on the preceding discussion. First, due to the difference in dielectric constant between the composite aerogel and the air, a small portion of the electromagnetic wave will not enter the aerogel and will continue propagating due to resistance when it comes into contact with the aerogel's surface. The layered porous structure within the composite aerogel allows for internal multiple reflections of electromagnetic waves, while defects in the graphene aerogel itself attenuate electromagnetic waves via dipole polarization. On this basis, the addition of Ag NWs improves the conductive network by introducing a significant amount of heterogeneous interfaces, allowing the aerogel to dissipate electromagnetic waves more effectively. In addition, the introduced $CoFe_2O_4$ NPs not only form a heterogeneous interface with the composite aerogel, enhancing the interfacial polarization and dipole polarization of the composite, but also more effectively absorb electromagnetic waves due to the exchange resonance and eddy current effect under the action of the electromagnetic field, further optimizing the composite aerogel's EMI shielding performance. In a word, Ag NWs may create an efficient conducting network and enhance the conductive loss of the composite aerogel, while $CoFe_2O_4$ NPs can introduce magnetic loss and improve the composite aerogel's electromagnetic wave absorption. The incorporation of Ag NWs and $CoFe_2O_4$ NPs facilitates the dielectric-magnetic synergy effect in the graphene composite aerogel, hence improving the attenuation pathway and finally enabling effective electromagnetic wave absorption.

As mentioned above, the multifunctionality is critical for the EMI shielding materials to meet the requirements of complicated application scenarios. Therefore, the multifunctionality of the $CoFe_2O_4$ NPs/Ag NWs/graphene aerogel is also investigated in this work. We evaluate the hydrophobic property of the $CoFe_2O_4$ NPs/Ag NWs/graphene aerogel via the measurement of water contact angle (Figs. 5(a) and 5(b)). After heat treatment, the composite aerogel shows remarkable hydrophobic property, while the contact angle is 120.3°. The hydrophobicity is attributed to the heat treatment, which removed the oxygen-containing functional groups from the surface of the graphene oxide. Excellent hydrophobicity of electromagnetic shielding materials can prevent them from accumulating water and corrosion in a humid environment, affecting their long-term reliability [60–62]. Moreover, the Joule heating property of the composite aerogel is also investigated. Figure 5(c) depicts the $T$–$U^2$ curve for the composite aerogel sample. The sample's $T$–$U^2$ curve is linear, indicating not only that it has stable resistance and conforms to Ohm's law, but also that it is controllable in terms of electric heating performance. As demonstrated in Fig. 5(d), the sample's temperature quickly achieves saturation once the driving voltage is supplied and stay stable there. After removing the driving voltage, the sample's temperature can be quickly reduced from saturation to room temperature, indicating that the composite aerogel not only has controllable electric heating performance but also good heat dissipation performance, which is particularly advantageous to the dissipation of heat energy generated by consuming electromagnetic wave energy in the electromagnetic shielding process [63–65]. The capacity to quickly dissipate heat energy efficiently prevents the impact of local overheating on performance and is also helpful for prolonged usage of the material. Figure 5(e) presents infrared pictures that intuitively indicate the sample's saturation temperature at various voltages. The figure demonstrates that the sample's temperature increases rapidly as the driving voltage increases, suggesting that the sample's electric heating capability is adjustable. Figure 5(f) describes the fluctuation of the composite aerogel sample's saturation temperature when the driving voltage is adjusted. It can be seen that as the driving voltage increases (6–10 V), the sample's saturation temperature rapidly rises from 45 to 120 °C, implying that it has a good Joule heat effect and can effectively convert electrical energy to thermal energy. This allows the material to work in extremely low temperatures. Meanwhile, when the driving voltage is varied between 6 and 10 V, the sample's temperature can be quickly switched between 45 and 120 °C. The sample can achieve the ideal saturation temperature within 2 s of increasing the voltage in this process, suggesting that the composite aerogel responds extremely quickly to electrically driven heat conversion. To examine the long-term stability of the electrothermal performance of the composite aerogel, we performed a 1 h electrothermal performance test at 9 V, as shown in Fig. 5(g). It is apparently that the sample can quickly achieve the

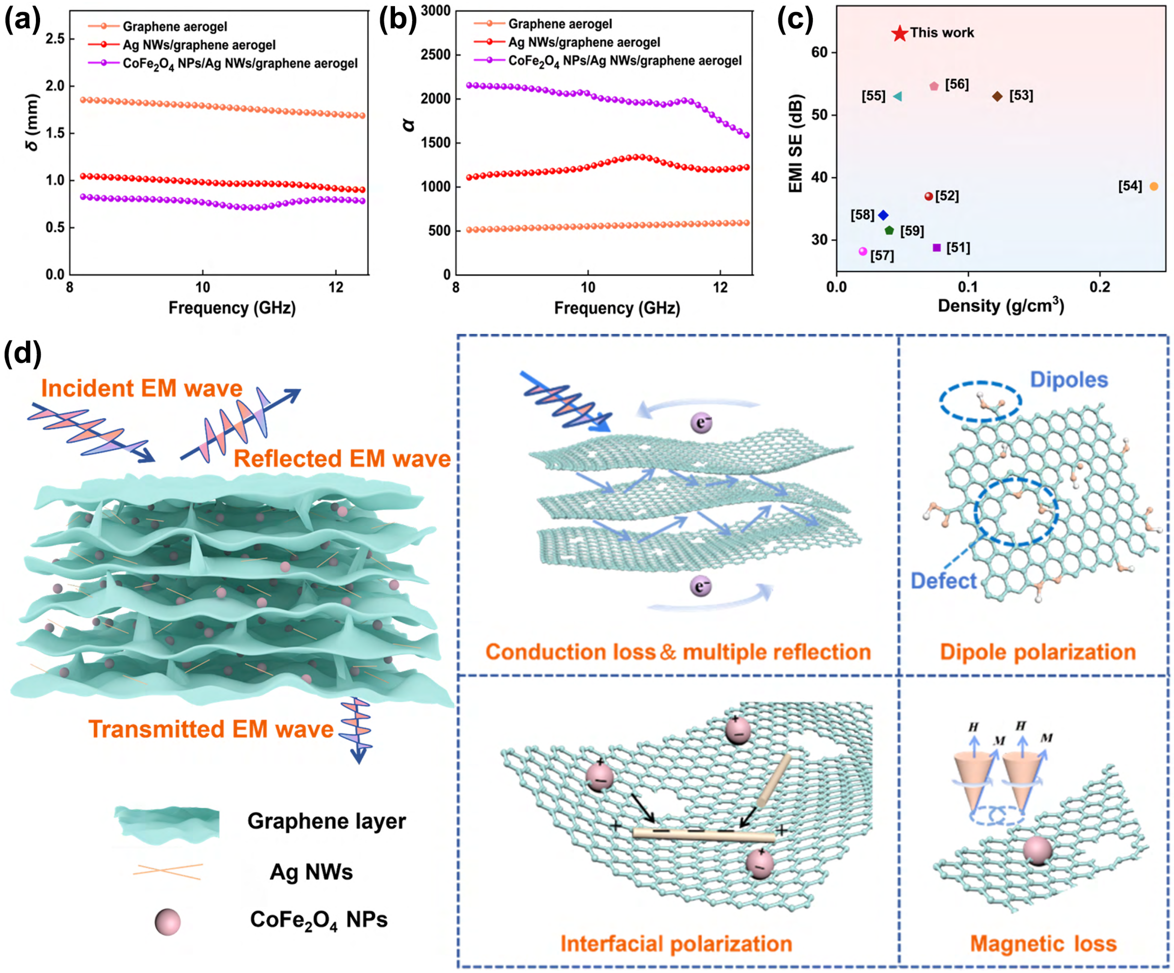


**Figure 4** (a) Attenuation constant and (b) skin depth of the as-prepared aerogel samples. (c) EMI shielding performance comparison of the $CoFe_2O_4$ NPs/Ag NWs/graphene aerogel with reported graphene aerogels. (d) Diagram of the shielding mechanism of the $CoFe_2O_4$ NPs/Ag NWs/graphene aerogel.

saturation temperature of 95 °C with a driving voltage of 9 V. During the 1h electric heating procedure, the sample's temperature can be kept stable around saturation, and it can be quickly decreased to room temperature after the driving voltage is removed.

## 4 Conclusion

In conclusion, we propose a $CoFe_2O_4$ NPs/Ag NWs/graphene aerogel for efficient and multifunctional EMI shielding. The $CoFe_2O_4$ NPs/Ag NWs/graphene aerogel delivers superior performance due to the realization of dielectric-magnetic synergy effect. The results reveal that Ag NWs improve the conductive network within the graphene aerogel while also increasing conductive loss. Meanwhile, the abundant heterogeneous interfaces created by the incorporation of Ag NWs and $CoFe_2O_4$ NPs enhance the composite aerogel's interfacial and dipole polarizations. More crucially, the presence of $CoFe_2O_4$ NPs induces magnetic loss in the composite aerogel. The $CoFe_2O_4$ NPs/Ag NWs/graphene aerogel with a thickness of 5 mm has a maximum $SE_T$ of more than 67.4 dB, which is 247% of graphite aerogel. Meanwhile, it exhibits a remarkable low density of 0.048 g/cm$^3$ and a high SSE value of up to 1291.67 dB·cm$^3$/g. Furthermore, it also demonstrates excellent Joule heating performance and hydrophobicity. This opens up the possibility of applying it in electromagnetic shielding in hostile situations. This research aims to provide guidelines for the development and construction of new EMI shielding materials that feature high efficiency and multifunctionality.

**Electronic Supplementary Material**: Supplementary material (SEM images of flake graphite and XRD spectra of Ag NWs and $CoFe_2O_4$ NPs) is available in the online version of this article at https://doi.org/10.26599/NR.2026.94908554.

## Data availability

All data needed to support the conclusions in the paper are presented in the manuscript and the Electronic Supplementary Material. Additional data related to this paper may be requested from the corresponding author upon request.

## Acknowledgements

The authors thank the financial support from the project funded by the National Natural Science Foundation of China (Nos. 52571231 and 52371198) and the Constructing National Independent Innovation Demonstration Zones (No. XM2024XTGXQ05).

## Declaration of competing interest

All the contributing authors report no conflict of interests in this work.

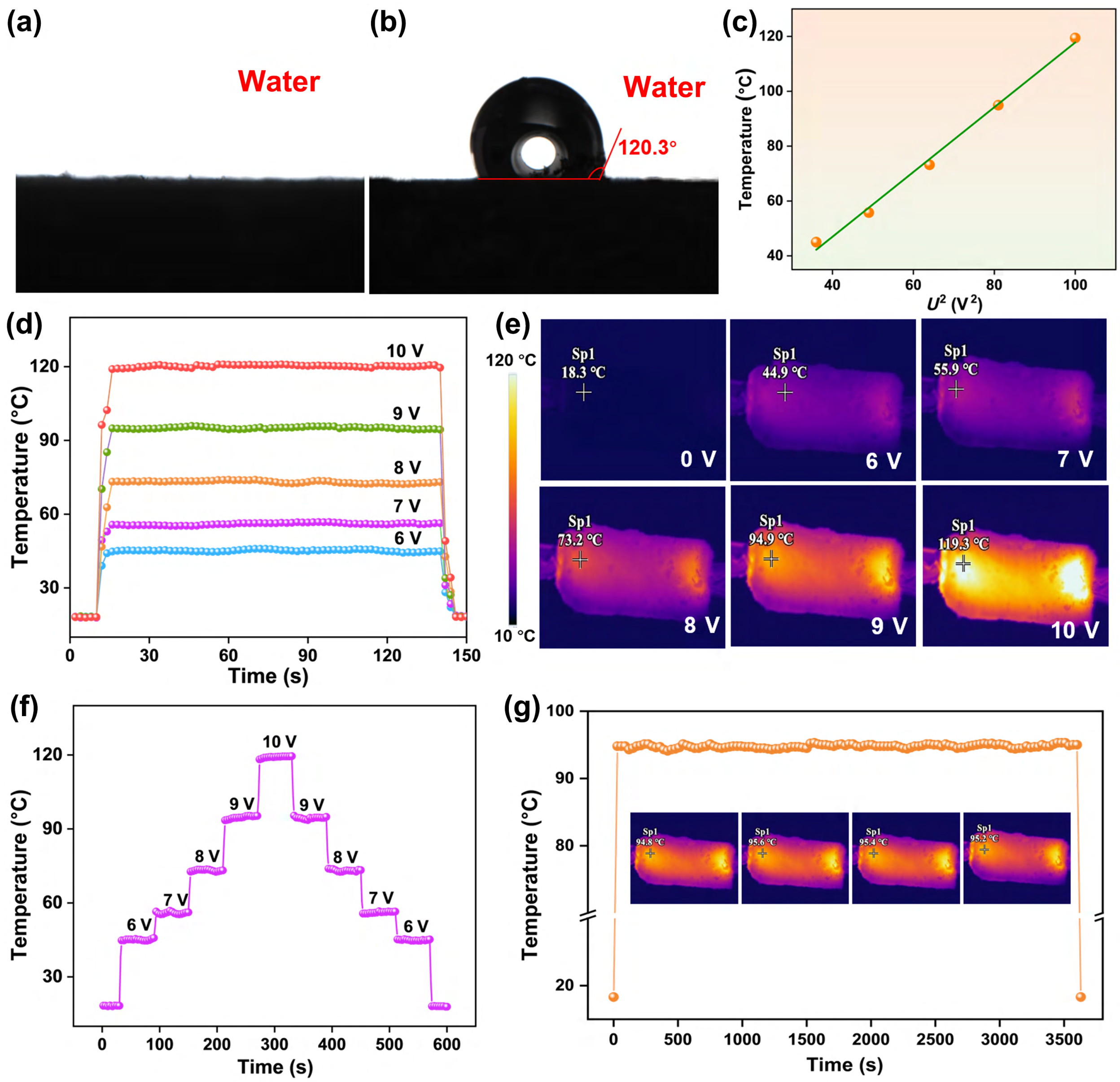


**Figure 5** Water contact angle of the $CoFe_2O_4$ NPs/Ag NWs/graphene aerogel: (a) before and (b) after the heat treatment. (c) Experimental data and linear fitting diagram of saturation temperature and $U^2$, (d) temperature vs. time curves under different voltages, (e) infrared images of saturation temperature under different voltages, and (f) saturation temperature evolution profile during voltage regulation of the $CoFe_2O_4$ NPs/Ag NWs/graphene aerogel. (g) Temperature profile of the $CoFe_2O_4$ NPs/Ag NWs/graphene aerogel at 9 V for 1 h.

## Author contribution statement

X. C. D.: Data curation, experimental design, writing – original draft. H. G. L.: Conceptualization, funding acquisition, writing – review & editing. Y. W. S.: Characterization. N. T. and C. Y. Y.: Funding acquisition, supervision. All the authors have approved the final manuscript.

## Use of AI statement

None.

## References

[1] Wang, J. E.; Ming, W.; Chen, L. F.; Song, T. L.; Yele, M.; Zhang, H.; Yang, L.; Sarula, G.; Liang, B. L.; Yan, L. T. et al. $MoS_2$ lubricate-toughened MXene/ANF composites for multifunctional electromagnetic interference shielding. *Nano-Micro Lett.* **2025**, *17*, 36.

[2] Zhang, Y. L.; Liu, A.; Tian, Y. Y.; Tian, Y. J.; Qi, X. S.; Qiu, H.; He, M. K.; Zhou, K.; Gu, J. W. Direct-ink-writing printed aerogels with dynamically reversible thermal management and tunable electromagnetic interference shielding. *Adv. Mater.* **2025**, *37*, 2505521.

[3] Ming, W.; Yang, L.; Chen, H. X.; Fei, F.; Zhang, H.; Sarula, G.; Wang, J. H.; Wang, T. Y.; Jin, C. Z.; Liang, B. L. et al. High toughness MXene/ANF-CZIF67/ANF "magnetic-electric" Janus film for multifunctional low reflection electromagnetic interference shielding. *Nano Res.* **2025**, *18*, 94907621.

[4] Yu, Y. Y.; Liu, X. B.; Lu, D. Q.; Liu, T.; Li, Y. S.; Wu, Z. P. Recent progress in graphene based materials for high-performance electromagnetic shielding. *Carbon* **2025**, *236*, 120093.

[5] Liu, A.; Qiu, H.; Lu, X. H.; Guo, H.; Hu, J. W.; Liang, C. B.; He, M. K.; Yu, Z.; Zhang, Y. L.; Kong, J. et al. Asymmetric structural

MXene/PBO aerogels for high-performance electromagnetic interference shielding with ultra-low reflection. *Adv. Mater.* **2025**, *37*, 2414085.

[6] Yele, M.; Sarula, G.; Yang, J.; Yang, L.; Zhang, H.; Chen, L. F.; Zhang, X. M.; Wang, J. H.; Wang, T. Y.; Jin, C. Z. et al. Integrated structural-functional MXene-GNs/ANF flexible composite film with enhanced thermal conductivity and electromagnetic interference shielding performance. *J. Mater. Sci. Technol.* **2026**, *241*, 200–210.

[7] Tian, L.; Gu, H. D.; Zhang, Q. Q.; You, X.; Wang, M. M.; Yang, J. S.; Dong, S. M. Multifunctional hierarchical metamaterial for thermal insulation and electromagnetic interference shielding at elevated temperatures. *ACS Nano* **2023**, *17*, 12673–12683.

[8] Zhang, Y. L.; Ruan, K. P.; Zhou, K.; Gu, J. W. Controlled distributed $Ti_3C_2T_x$ hollow microspheres on thermally conductive polyimide composite films for excellent electromagnetic interference shielding. *Adv. Mater.* **2023**, *35*, 2211642.

[9] Meng, Y. T.; Cai, B.; Zhou, Y. T.; Zhou, L.; Zhang, Y.; Wang, J. H.; Sarula, G.; Yan, L. T.; Lu, M.; Liang, B. L. et al. Bionic coral reef inspired enhanced scattering of trimetallic LDH self assembled $Ti_3C_2T_x$ MXene for advanced microwave absorption. *Nano Res.* **2025**, *18*, 94907842.

[10] Wang, X. L.; Hu, X. P.; Liu, Z. G.; Zhu, C. B.; Shen, R.; Quan, B. Q.; Yan, X. Y.; Wang, W. L.; Lu, X.; Qu, J. P. Interpenetrating double-network ANF/MXene-$K^+$ aerogels enable integrated electromagnetic interference shielding, infrared camouflage, and Joule Heating in adaptive multifunctional systems. *Nano Res.* **2025**, *18*, 94907702.

[11] Zhai, M. Z.; Zhao, S. J.; Guo, H.; Li, X. C.; Shi, X. T.; He, M. K.; Zhang, Y. L.; Gu, J. W. Bionic-structured electromagnetic interference shielding composites. *Sci. Bull.* **2025**, *70*, 2347–2364.

[12] Wang, J. E.; Song, T. L.; Ming, W.; Yele, M.; Chen, L. F.; Zhang, H.; Zhang, X. J.; Liang, B. L.; Wang, G. S. High MXene loading, nacre-inspired MXene/ANF electromagnetic interference shielding composite films with ultralong strain-to-failure and excellent Joule heating performance. *Nano Res.* **2024**, *17*, 2061–2069.

[13] Hu, X. P.; Ai, B.; Quan, B. Q.; Shi, Z. J.; Liu, Z. G.; Sheng, M. J.; Ding, Y.; Yan, H.; Xiao, Y.; Lu, G. C. et al. Synergistically networked 1D/2D/3D phase change composites with Ultra-Fast contactless thermal energy conversion and enhanced electromagnetic interference shielding performance. *Chem. Eng. J.* **2025**, *504*, 158915.

[14] Liu, J.; Nicolosi, V. Electrically insulating electromagnetic interference shielding materials: A perspective. *Adv. Funct. Mater.* **2025**, *35*, 2407439.

[15] Ji, Q. H.; Sheng, X. X.; Li, X. L.; Liu, S.; Chen, Q. F.; Guo, P. Z.; Yang, Y. B.; Huang, Y. Y.; Zhang, G. L.; Lu, X. et al. Camel skin-fat structure inspired MXene@PVA/PCC aerogel composite for efficient medium and low temperature infrared stealth. *Chem. Eng. J.* **2023**, *476*, 146671.

[16] Liu, A.; Xu, X. S.; Qiu, H.; Guo, H.; He, M. K.; Yu, Z.; Zhang, Y. L.; Gu, J. W. Bioinspired hollow heterostructure fillers for enhanced electromagnetic interference shielding in polyimide aerogels. *InfoMat* **2025**, *7*, e70060.

[17] Luo, Y.; Guo, Y. B.; Wei, C.; Chen, J. W.; Zhao, G. Y.; Yuan, Q.; Zhu, Y. T. Lightweight, compressible, and stretchable composite foams for ultra-efficient and high-stable electromagnetic interference shielding materials. *Carbon* **2023**, *215*, 118480.

[18] Zhang, Y. L.; Gu, J. W. Ultrathin and flexible electromagnetic interference shielding films by interface-confinement strategy. *Sci. China Mater.*, in press, DOI: 10.1007/s40843-025-3876-5.

[19] Rajan, A.; Solaman, S. K.; Ganesanpotti, S. Electromagnetic simulation integrated strategy to metamorphose commercial cotton into multifunctional electromagnetic interference shielding fabrics. *Adv. Compos. Hybrid Mater.* **2025**, *8*, 203.

[20] Yao, W. Q.; Mao, R. W.; Gao, W. W.; Chen, W. Q.; Xu, Z.; Gao, C. Piezoresistive effect of superelastic graphene aerogel spheres. *Carbon* **2020**, *158*, 418–425.

[21] Wu, Y.; An, C.; Guo, Y. R.; Zong, Y. Y.; Jiang, N. S.; Zheng, Q. B.; Yu, Z. Z. Highly aligned graphene aerogels for multifunctional composites. *Nano-Micro Lett.* **2024**, *16*, 118.

[22] Ahmad, N.; Zhao, Y. J.; Zeng, K. X.; Zhai, W. Multifunctional aramid fiber–reinforced graphene aerogels with superior acoustic, thermal and strain sensing performance. *Carbon* **2026**, *252*, 121413.

[23] Wang, Z. Y.; Shen, X.; Han, N. M.; Liu, X.; Wu, Y.; Ye, W. J.; Kim, J. K. Ultralow electrical percolation in graphene aerogel/epoxy composites. *Chem. Mater.* **2016**, *28*, 6731–6741.

[24] Gao, W. W.; Zhao, N. F.; Yu, T.; Xi, J. B.; Mao, A. R.; Yuan, M. Q.; Bai, H.; Gao, C. High-efficiency electromagnetic interference shielding realized in nacre-mimetic graphene/polymer composite with extremely low graphene loading. *Carbon* **2020**, *157*, 570–577.

[25] Lin, Z.; Shen, C. W.; Xia, Y. X.; Ma, R. Z.; He, J.; Zhu, B. Y.; Liu, Y. J.; Xu, Z.; Gao, W. W.; Gao, C. Multifunctional layered structure graphene aerogel with customizable shape by ion diffusion-directed assembly. *Carbon* **2025**, *238*, 120265.

[26] He, Z. J.; Zhang, W. R.; Zhang, J.; Xie, J. L.; Su, F. F.; Li, Y. C.; Yao, D. D.; Wang, Y. D.; Zheng, Y. P. Enhancing the electromagnetic interference shielding of epoxy resin composites with hierarchically structured MXene/graphene aerogel. *Compos. Part B: Eng.* **2024**, *274*, 111230.

[27] Liang, L. Y.; Li, Q. M.; Yan, X.; Feng, Y. Z.; Wang, Y. M.; Zhang, H. B.; Zhou, X. P.; Liu, C. T.; Shen, C. Y.; Xie, X. L. Multifunctional magnetic $Ti_3C_2T_x$ MXene/graphene aerogel with superior electromagnetic wave absorption performance. *ACS Nano* **2021**, *15*, 6622–6632.

[28] Yang, X. Q.; Zhang, Y. F.; Luo, J. M.; Tusiime, R.; Lu, C. Z.; Xue, Y.; Zhou, J. L.; Liu, Y.; Zhang, H.; Yu, J. Y. $Fe_3O_4$ uniformly decorated reduced graphene oxide aerogel for epoxy nanocomposites with high EMI shielding performance. *Compos. Commun.* **2022**, *36*, 101391.

[29] Patel, M. A.; Yang, H.; Chiu, P. L.; Mastrogiovanni, D. D. T.; Flach, C. R.; Savaram, K.; Gomez, L.; Hemnarine, A.; Mendelsohn, R.; Garfunkel, E. et al. Direct production of graphene nanosheets for near infrared photoacoustic imaging. *ACS Nano* **2013**, *7*, 8147–8157.

[30] Lee, W. J.; Kim, C. S.; Yang, S. Y.; Lee, D.; Kim, Y. S. Spontaneous exfoliation of large-sized graphene oxide with low defect concentration by simple wet chemistry. *Carbon* **2021**, *182*, 214–222.

[31] Guo, M. H.; Yuan, H.; Ni, K.; Ye, C. R.; Pan, F.; Xiong, J.; Zhu, Y. W. Structural repair of reduced graphene oxide promoted by single-layer graphene. *Adv. Sci.* **2025**, *12*, 2410088.

[32] Zhang, Y.; Gao, Q.; Zhang, S.; Fan, X.; Qin, J. B.; Shi, X. T.; Zhang, G. C. rGO/MXene sandwich-structured film at spunlace non-woven fabric substrate: Application to EMI shielding and electrical heating. *J. Colloid Interface Sci.* **2022**, *614*, 194–204.

[33] Jiang, C.; Wen, B. Y. Construction of 1D heterogeneous Co/C@Ag Nws with tunable electromagnetic wave absorption and shielding performance. *Small* **2023**, *19*, 2301760.

[34] Wang, X. Y.; Lu, Y. K.; Zhu, T.; Chang, S. C.; Wang, W. $CoFe_2O_4$/N-doped reduced graphene oxide aerogels for high-performance microwave absorption. *Chem. Eng. J.* **2020**, *388*, 124317.

[35] Wang, R.; Xu, H. Y.; Chu, G. Y.; Nie, Z. G.; Peng, Y. M.; Zhao, Z. Y.; Jiang, F. J.; Jiang, M. Y.; Qi, S. H.; Wang, R. M. Rigid and lightweight $CoFe_2O_4$/carbon nanofibers/polyimide composite aerogel with anisotropic structure for efficient microwave absorption and thermal insulation. *Compos. Sci. Technol.* **2026**, *273*, 111422.

[36] Saeed, M. U.; Weng, Y. K.; Bahzad, M.; Shin, S.; Aaron, D. S.; Kihm, K. D. Structural formation and pore control of freeze-cast directional graphene aerogel (DGA). *ACS Appl. Mater. Interfaces* **2024**, *16*, 425–434.

[37] Min, P.; Li, X. F.; Liu, P. F.; Liu, J.; Jia, X. Q.; Li, X. P.; Yu, Z. Z. Rational design of soft yet elastic lamellar graphene aerogels via bidirectional freezing for ultrasensitive pressure and bending sensors. *Adv. Funct. Mater.* **2021**, *31*, 2103703.

[38] Sun, M. H.; Wang, Z. P.; Xiao, J. W.; Tian, X.; Ma, X.; Wang, S. AgNWs/$Fe_3O_4$@NC conductive network hierarchical assembly to

prepare flexible EMI shielding textile. *Small* **2024**, *20*, 2304622.
[39] Deng, S. W.; Dai, M. Y.; Fang, B. D.; Huang, Y. Q.; Zeng, S. L.; Huang, Z. N.; Xue, J. H.; Li, X. D.; Shi, S. H.; Cheng, F. C. Assembly of PAN/Gr@MWCNTs/$CoFe_2O_4$ multilayer composite films for high-efficiency electromagnetic shielding and Joule heating. *Compos. Sci. Technol.* **2025**, *262*, 111081.
[40] Hu, X. F.; Zhang, Y. L.; Guo, H.; He, M. K.; Qiu, H.; Shi, X. T.; Wang, L.; Gu, J. W. Multifunctional flexible WPU composite aerogels with sandwich structure for dual-sided low-reflection electromagnetic interference shielding. *Adv. Funct. Mater.* **2026**, *36*, e17665.
[41] Somesh, T. E.; Balamurugan, S.; Son, W.; Zhao, J. H.; Tran, D. T.; Kim, N. H.; Lee, J. H. Triphasic ATH@rGO-$CoFe_2O_4$ hybrid nanofiller-integrated waterborne polyurethane composites for dual functionality: Fire retardancy and EMI shielding. *Nanoscale* **2025**, *17*, 16503–16514.
[42] Liu, H. Z.; Xu, Y.; Yang, K.; Han, D.; Yong, H. Y.; Yang, Q. W. Alternating current assisted preparation of three-dimensional graphene aerogels and the application in electromagnetic interference shielding. *Mater. Today Phys.* **2024**, *40*, 101308.
[43] Wan, Y. J.; Zhu, P. L.; Yu, S. H.; Sun, R.; Wong, C. P.; Liao, W. H. Ultralight, super-elastic and volume-preserving cellulose fiber/graphene aerogel for high-performance electromagnetic interference shielding. *Carbon* **2017**, *115*, 629–639.
[44] Cao, Y. S.; Cheng, Z.; Wang, R. F.; Liu, X. Y.; Zhang, T. R.; Fan, F.; Huang, Y. Multifunctional graphene/carbon fiber aerogels toward compatible electromagnetic wave absorption and shielding in gigahertz and terahertz bands with optimized radar cross section. *Carbon* **2022**, *199*, 333–346.
[45] Lalan, V.; Ganesanpotti, S. The smallest anions entrapped mayenite electride@graphitic carbon core–shells reinforced with superparamagnetic $Fe_3O_4$ delivers unrivalled high-frequency microwave absorption. *Chem. Eng. J.* **2023**, *461*, 141857.
[46] Qi, J. M.; Liang, C. B.; Ruan, K. P.; Li, M. K.; Guo, H.; He, M. K.; Qiu, H.; Guo, Y. Q.; Gu, J. W. Cactus-like architecture for synergistic microwave absorption and thermal management. *Natl. Sci. Rev.* **2025**, *12*, nwaf394.
[47] Han, Y. X.; Yang, Y. R.; Li, T. H.; Zhang, Y. L.; Guo, H.; He, M. K.; Han, K. H.; Qiu, H.; Gu, J. W. Hierarchical heterogeneous co-based magnetic absorbers for superior broadband high-efficiency microwave absorption. *Adv. Funct. Mater.*, in press, DOI: 10.1002/adfm.202525719.
[48] He, M. K.; Zhong, X.; Lu, X. H.; Hu, J. W.; Ruan, K. P.; Guo, H.; Zhang, Y. L.; Guo, Y. Q.; Gu, J. W. Excellent low-frequency microwave absorption and high thermal conductivity in polydimethylsiloxane composites endowed by hydrangea-like CoNi@BN heterostructure fillers. *Adv. Mater.* **2024**, *36*, 2410186.
[49] Huang, M. Q.; Li, B. X.; Qian, Y. T.; Wang, L.; Zhang, H. B.; Yang, C. D.; Rao, L. J.; Zhou, G.; Liang, C. Y.; Che, R. C. MOFs-derived strategy and ternary alloys regulation in flower-like magnetic-carbon microspheres with broadband electromagnetic wave absorption. *Nano-Micro Lett.* **2024**, *16*, 245.
[50] Wang, Y. Y.; Zhang, F.; Li, N.; Shi, J. F.; Jia, L. C.; Yan, D. X.; Li, Z. M. Carbon-based aerogels and foams for electromagnetic interference shielding: A review. *Carbon* **2023**, *205*, 10–26.
[51] Yu, Z.; Dai, T. W.; Yuan, S. W.; Zou, H. W.; Liu, P. B. Electromagnetic interference shielding performance of anisotropic polyimide/graphene composite aerogels. *ACS Appl. Mater. Interfaces* **2020**, *12*, 30990–31001.
[52] Song, W. L.; Guan, X. T.; Fan, L. Z.; Cao, W. Q.; Wang, C. Y.; Cao, M. S. Tuning three-dimensional textures with graphene aerogels for ultra-light flexible graphene/texture composites of effective electromagnetic shielding. *Carbon* **2015**, *93*, 151–160.
[53] Han, D.; Zhao, Y. H.; Bai, S. L.; Ping, W. C. High shielding effectiveness of multilayer graphene oxide aerogel film/polymer composites. *RSC Adv.* **2016**, *6*, 92168–92174.
[54] Narasimman, R.; Vijayan, S.; Prabhakaran, K. Graphene-reinforced carbon composite foams with improved strength and EMI shielding from sucrose and graphene oxide. *J. Mater. Sci.* **2015**, *50*, 8018–8028.
[55] Wang, L.; Shi, X. T.; Zhang, J. L.; Zhang, Y. L.; Gu, J. W. Lightweight and robust rGO/sugarcane derived hybrid carbon foams with outstanding EMI shielding performance. *J. Mater. Sci. Technol.* **2020**, *52*, 119–126.
[56] Jiang, X. Y.; Zhao, Z. X.; Zhou, S. T.; Zou, H. W.; Liu, P. B. Anisotropic and lightweight carbon/graphene composite aerogels for efficient thermal insulation and electromagnetic interference shielding. *ACS Appl. Mater. Interfaces* **2022**, *14*, 45844–45852.
[57] Wang, Y. Y.; Sun, W. J.; Yan, D. X.; Dai, K.; Li, Z. M. Ultralight carbon nanotube/graphene/polyimide foam with heterogeneous interfaces for efficient electromagnetic interference shielding and electromagnetic wave absorption. *Carbon* **2021**, *176*, 118–125.
[58] Lee, J. S.; Kim, J. W.; Lee, J. H.; Son, Y. K.; Kim, Y. B.; Woo, K.; Lee, C.; Kim, I. D.; Seok, J. Y.; Yu, J. W. et al. Flash-induced high-throughput porous graphene via synergistic photo-effects for electromagnetic interference shielding. *Nano-Micro Lett.* **2023**, *15*, 191.
[59] Li, Y.; Chen, J. X.; Cai, P. W.; Wen, Z. H. An electrochemically neutralized energy-assisted low-cost acid-alkaline electrolyzer for energy-saving electrolysis hydrogen generation. *J. Mater. Chem. A* **2018**, *6*, 4948–4954.
[60] Xu, Y. J.; Hou, M. H.; Wang, J. Porous gradient composite with dependable superhydrophobic protection for multifunctional electromagnetic interference shielding. *ACS Appl. Mater. Interfaces* **2024**, *16*, 3978–3990.
[61] Luo, J. C.; Wang, L.; Huang, X. W.; Li, B.; Guo, Z.; Song, X.; Lin, L. W.; Tang, L. C.; Xue, H. G.; Gao, J. F. Mechanically durable, highly conductive, and anticorrosive composite fabrics with excellent self-cleaning performance for high-efficiency electromagnetic interference shielding. *ACS Appl. Mater. Interfaces* **2019**, *11*, 10883–10894.
[62] Hu, H.; Zhao, Z. B.; Wan, W. B.; Gogotsi, Y.; Qiu, J. S. Ultralight and highly compressible graphene aerogels. *Adv. Mater.* **2013**, *25*, 2219–2223.
[63] Li, M.; Zheng, Y.; Bai, H.; Gao, W. W. Advances in ice-templated graphene aerogels: Fabrication, properties, and applications. *ACS Appl. Mater. Interfaces* **2025**, *17*, 19247–19262.
[64] Quan, L.; Wang, C. H.; Xu, Y. L.; Qiu, J. L.; Zhang, H. Y.; Cunning, B.; Huang, M.; Wei, H. J.; Seong, W. K.; Seo, J. et al. Electromagnetic properties of graphene aerogels made by freeze-casting. *Chem. Eng. J.* **2022**, *428*, 131337.
[65] Afroze, J. D.; Abden, M. J.; Yuan, Z. W.; Wang, C. J.; Wei, L.; Chen, Y.; Tong, L. Y. Core–shell structured graphene aerogels with multifunctional mechanical, thermal and electromechanical properties. *Carbon* **2020**, *162*, 365–374.